


**DFT study of the electronic properties and the cubic to tetragonal phase transition in RbCaF<sub>3</sub>**

Sohaib Ehsan, Andreas Tröster, Fabien Tran, and Peter Blaha

*Institute of Materials Chemistry, Vienna University of Technology, Getreidemarkt 9/165-TC, A-1060 Vienna, Austria* (Received 3 April 2018; revised manuscript received 4 July 2018; published 28 September 2018)

The structural, elastic, vibrational, and electronic properties of RbCaF<sub>3</sub> in the cubic and low-temperature tetragonal phases have been studied at the *ab initio* level with density functional theory. Using various exchange-correlation functionals of the generalized gradient approximation for structural properties like the CaF<sub>6</sub> octahedron rotational angle or ratio  $c/a$  of the tetragonal lattice constants, it is found that the best agreement with experiment is obtained with the PBEsol and Wu and Cohen (WC) functionals. The fundamental band gap is calculated to be direct and indirect in the tetragonal and cubic phases, respectively. The relation between the cubic and tetragonal phases is studied by monitoring the cubic zone boundary soft mode phonon  $R_{15'}$  as well as the  $c/a$  ratio and tilt angle. The results for the Born effective charge tensors are also reported in order to study the effect of the long-range Coulomb interactions. We also investigated the corresponding pressure driven phase transition at  $T = 0$  K, which we observe to be of second order in contrast to the first-order character experimentally detected for the structurally similar high pressure transition at ambient temperature. Based on recently developed finite strain Landau theory, we offer a possible explanation for this peculiar change of character.

DOI: [10.1103/PhysRevMaterials.2.093610](https://doi.org/10.1103/PhysRevMaterials.2.093610)**I. INTRODUCTION**

Materials of the perovskite family have been extensively studied for many decades, but still continue to attract great attention [1,2]. Despite its simplicity, the perovskites structure can undergo a large variety of structural phase transitions with respect to temperature and/or pressure, thus giving rise to a rich spectrum of interesting physical properties with corresponding technological applications. As to fluoride based perovskites, we mention their interesting optical properties [3–5] and the occurrence of high-temperature ferroelectricity [6], although without stereochemically active atoms ferroelectricity is not to be expected in the present case. Due to its wide band gap, RbCaF<sub>3</sub> can be used as a vacuum-ultraviolet-transparent material for lenses in optical lithography steppers [7].

Similar to what is found in many other perovskites, on lowering the temperature at ambient pressure, RbCaF<sub>3</sub> undergoes a series of temperature-induced phase transitions in which the parental cubic  $Pm\bar{3}m$  aristotype symmetry [8] is lowered by octahedral tilting [9]. The first cubic-tetragonal transition in this sequence is structurally similar to the ones in SrTiO<sub>3</sub> and KMnF<sub>3</sub> (see Refs. [10–13]). These types of perovskites undergo a second-order antiferrodistortive (AFD) phase transition to space group symmetry  $I4/mcm$  due to the rotation of CaF<sub>6</sub> octahedra around the cubic  $z$  axis related to the softening of the triply degenerate  $R_{15'}$  phonon mode in the cubic Brillouin zone (BZ). For RbCaF<sub>3</sub> this transition was extensively studied experimentally by a number of authors. Depending upon the experimental techniques used like Raman scattering [14,15], x-ray diffraction [16–19], specific-heat measurements [20], neutron-scattering [21–23], or thermal conductivity [24], this cubic-to-tetragonal phase transition is observed with reported transition temperatures

varying between approximately 193 and 199 K. In parallel to the case of, e.g., SrTiO<sub>3</sub>, a recent study of RbCaF<sub>3</sub> showed that at room temperature, a structurally similar transition can also be triggered by application of hydrostatic pressure, but the resulting transition at 2.8 GPa is reported to be of first rather than of second order [23].

The subsequent temperature-driven phase transition from tetragonal to orthorhombic symmetry is much less studied in comparison to the former one. In the Raman study of both ambient pressure transitions (cubic→tetragonal→orthorhombic) [14], a first-order transition to  $Pnma$  symmetry is reported at around 31.5 K.

As to theoretical approaches, there are a number of *ab initio* calculations for the cubic phase of RbCaF<sub>3</sub> [25–27,27,28] but, to the best of our knowledge, neither the tetragonal phase nor results of density functional theory (DFT) based phonon calculations have been published up to date. It is the purpose of the present work to provide a thorough *ab initio* investigation of structural, elastic, vibrational, and electronic properties of RbCaF<sub>3</sub> in both, the cubic and the tetragonal phase. Special emphasis will be given to the pressure induced phase transition between these two phases.

This paper is organized as follows. In Sec. II, the computational details are given. Sections III, IV, and V are devoted to the structural, electronic, and elastic properties, respectively, while the vibrational properties are discussed in Sec. VI and the born effective charges in Sec. VII. The continuous (i.e., second-order) nature of the pressure-driven phase transition we detect at zero temperature as opposed to the first-order character of the experimentally observed high-pressure phase transition at ambient temperature can be understood within the framework of the recently developed finite strain Landau theory [29,30], as is argued in Sec. VIII. Finally, the conclusions are summed up in Sec. IX.

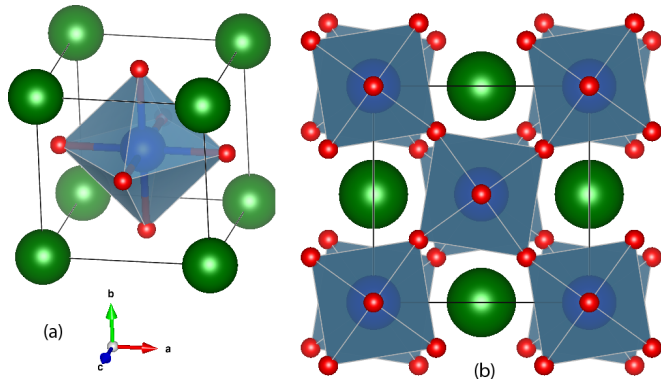


FIG. 1. Structures of the (a) cubic and (b) tetragonal phases of  $\text{RbCaF}_3$ , where green, blue, and red colors represent Rb, Ca, and F atoms, respectively. Note that the conventional tetragonal cell is  $\sqrt{2} \times \sqrt{2} \times 2$  larger than the cubic cell (although we actually use a two times smaller body-centered cell) and the tilt angle  $\phi$  is clearly visible.

## II. THEORY AND COMPUTATIONAL DETAILS

The *ab initio* calculations were performed with the WIEN2K code [31], which is based on the (linearized) augmented plane-wave and local orbitals [(L)APW+lo] method to solve the Kohn-Sham equations [32] of DFT. Here, we content ourselves with sketching the main ideas of this approach (see, e.g., Ref. [33] for more details). In the (L)APW+lo method, the unit cell of the crystal is divided into atomic spheres surrounding the nuclei and the remaining interstitial region. Inside the atomic spheres, the wave functions are expanded with atomiclike basis functions, i.e., numerical radial functions times spherical harmonics while, in contrast, within the interstitial region the basis functions are plane waves. These two regions are connected by requiring continuity of the basis functions (and their first derivative depending on the flavor of the (L)APW+lo method) across the sphere boundary.

The cubic  $Pm\bar{3}m$  unit cell of  $\text{RbCaF}_3$  contains five atoms [Fig. 1(a)]: Rb at the Wyckoff position 1a (0, 0, 0), Ca at 1b (0.5, 0.5, 0.5), and F at 3c (0.5, 0.5, 0). During the cubic  $\rightarrow$  tetragonal transition, the  $\text{CaF}_6$  octahedra are rotated along one of the cubic axes, which for definiteness we take to be the  $z$  axis. With respect to the  $x$  and  $y$  axis, the octahedra thus appear to be tilted, the tilt angle  $\phi$  serving as an order parameter for the transition. Since the tilts occur in an alternating fashion for neighboring cells, the transition is accompanied by a doubling of the primitive unit cell, whose conventional  $x$  and  $y$  axes are rotated by  $45^\circ$  and stretched by a factor of  $\sqrt{2}$  with respect to the parent cubic cell. Along the  $z$  axis, the rotations/tilts occur in an alternating fashion [Fig. 1(b)], which also implies a doubling of the conventional lattice parameter  $c$ . The resulting conventional body-centered tetragonal  $I4/mcm$  unit cell hosts 20 atoms with four nonequivalent sites: Rb sits at 4b (0, 0.5, 0.25), Ca at 4c (0, 0, 0), F1 at 4a (0, 0, 0.25), and the other F3 at 8h ( $u + 0.25, u + 0.75, 0$ ), where  $u$  is a free parameter. Lattice periodicity in the tetragonal phase along the rotated  $x$  and  $y$  directions is described by the lattice constant  $a\sqrt{2}$ , whereas the periodicity along  $z$  is close to twice the lattice constant of the cubic phase. The ratio  $c/a$  (for simplicity we will use  $c/a$  instead of  $c/\sqrt{2}a$ ) of

pseudocubic lattice constants is commonly taken as a measure of the tetragonal distortion. Note, however, that in the actual calculation primitive cells are used.

Since the energy gain due to the AFD phase transition is very small, particular care in the choice of the parameters of the calculations was taken in order to properly converge the total energy and forces. For instance,  $7 \times 7 \times 7$  and  $10 \times 10 \times 10$   $k$  meshes were used and found sufficient for the tetragonal and cubic primitive unit cells, respectively. Also of crucial importance is the size of the basis set, which is controlled by the product of the smallest of the atomic sphere radii  $R_{\text{MT}}^{\text{min}}$  and the plane-wave cutoff  $K_{\text{max}}$ . The calculations of the present work were done with  $R_{\text{MT}}^{\text{min}}K_{\text{max}} = 9$  and atomic sphere radii of 2.2, 1.9, and 1.9 bohr for Rb, Ca, and F, respectively.

In DFT, the reliability of the results usually depends on the approximate exchange-correlation (XC) functional that is chosen for the calculations [34,35]. Therefore it is important to choose, to the extent it is possible, an approximation that is suited for the problem and property under study. In the present work, we considered the local density approximation (LDA) [36] and three functionals of the generalized gradient approximation, namely, PBE from Perdew *et al.* [37], and its solid-state optimized version PBEsol [38] and WC from Wu and Cohen [39]. On average, LDA and PBE are known to underestimate and overestimate the lattice constants of solids, respectively, while PBEsol and WC produce more accurate results in between LDA and PBE [40,41]. Additionally, we also report calculations with the modified Becke-Johnson potential [42] (mBJ) for the electronic properties. The mBJ potential, which depends on the kinetic-energy density and is therefore of the meta-GGA class, is well known [43–45] to give significantly improved band gaps compared to standard GGA functionals like those considered in the present work.

## III. STRUCTURAL PROPERTIES

In order to calculate structural properties like the lattice constants and bond lengths, the first step consists of determining the unit cell dimensions at vanishing hydrostatic pressure. For the cubic phase, this merely amounts to calculating the total energy as a function of the lattice constant  $a$  and fitting the energy values with a Birch-Murnaghan equation of state [47]. Table I shows the results of our calculations for the equilibrium lattice constant  $a_0$ , the bulk modulus  $B$ , and its pressure derivative  $B'$  that were obtained with the different XC functionals. For comparison purposes, experimental values as well as previous DFT results are also displayed in Table I. As commonly obtained with LDA, the equilibrium lattice constant is too short (by 0.1 Å) compared to experiment, while PBE shows the opposite trend ( $a_0$  too large by 0.07 Å). As expected [29,30], both, PBEsol and WC, improve the agreement with experiment, since their values for  $a_0$  are 4.444 and 4.449 Å, respectively, which basically coincide with the experimental value 4.448 Å [16]. The same conclusion is reached for the bulk modulus  $B$ , since PBEsol (52.5 GPa) and WC (50.8 GPa) also lead to excellent agreement with experiment (50 GPa), while LDA and PBE lead to overestimation and underestimation, respectively. Compared to the other theoretical works, our results for LDA, PBE, and WC are

TABLE I. Structural properties and band gap of the cubic phase of RbCaF<sub>3</sub>.

	Present work					Other works				
	LDA	PBE	PBEsol	WC	mBJ	LDA	PBE	WC	mBJ	Expt.
$a_0$ (Å)	4.355	4.522	4.444	4.449		4.349 [27], 4.34 [28]	4.353 [26], 4.514 [27]	4.452 [25]		4.448 [16]
$B$ (GPa)	64.1	46.7	52.5	50.8		62.96 [27], 57.88 [28]	61.9 [26], 46.72 [27]	49.77 [25]		50.03 [23]
$B'$	4.8	4.6	4.8	4.9			4.12 [26]	5.0 [25]		4.2 [23]
Band gap (eV)	6.62	6.40	6.50	6.58	10.46	6.629 [27], 6.79 [28]	6.6 [26], 6.40 [27], 6.65 [28]		10.88 [28]	10.9 [46]

in agreement with the values in Refs. [25,27]. However, the PBE results from Ref. [26] differ significantly from ours and are, curiously, much more similar to the LDA results. The calculations in the tetragonal phase are somewhat more involved than those in the cubic phase, since for each unit cell volume the ratio  $c/a$  of the unit cell parameters and the free parameter  $u$  of the F atom at Wyckoff position 8h (determining the tilt angle of the fluorine octahedra) have to be optimized. Since PBEsol (and WC) was shown to be more accurate than the other functionals for the cubic phase, the calculations in the tetragonal phase were done only with PBEsol. The results for the tetragonal structure are shown in Table II, which also contains experimental results. The theoretical unit cell volume obtained from our calculation is found to be only 0.4% smaller than the experimental value, while most other quantities, e.g.,  $c/a$ , the Ca-F bond length, and the bulk modulus are also in good agreement with experiment. We just note that the PBEsol and experimental values for the  $\text{CaF}_6\angle$  differ slightly ( $9.31^\circ$  for PBEsol versus  $7.96^\circ$  for experiment).

Figure 2(a) compares the PBEsol equation of state of the cubic and tetragonal phases, where we can see that the tetragonal structure has a lower total energy and is therefore more stable than the cubic one. Nevertheless, as the volume increases, the energy difference between both phases decreases and at a volume of  $99 \text{ \AA}^3$  the two curves merge and the phase transition between the cubic and tetragonal structures occurs. Numerically, the transition volume, which translates into a negative pressure of  $-4.8 \text{ GPa}$ , is more clearly determined from monitoring the variation of the  $c/a$  ratio and tilt angle

TABLE II. Structural properties and band gap of the tetragonal phase of RbCaF<sub>3</sub> calculated with the PBEsol functional. The band gap calculated with the mBJ potential is also shown.  $\text{CaF}_6\angle$  is a measure of the tilting of the  $\text{CaF}_6$  octahedra.

	Present work	Expt.
$a_0$ (Å)	6.235	6.251 (55 K) [16]
$c_0$ (Å)	8.941	8.933 (55 K) [16]
$B$ (GPa)	49.3	
$c/(\sqrt{2}a)$	1.014	1.0105 (55 K) [16]
$u$	0.041	0.035 (55 K) [16]
$\text{CaF}_6\angle$	$9.31^\circ$	$7.96^\circ$ (55 K) [16]
Rb-F1 (Å)	3.117	
Rb-F3 (Å)	2.899	
Ca-F1 (Å)	2.235	2.2405 (87.5 K) [16]
Ca-F3 (Å)	2.233	2.2395 (87.5 K) [16]
Band gap (eV)	6.63 (mBJ: 10.58)	

of the rotation of the  $\text{CaF}_6$  octahedra with volume as shown in Fig. 2(b). At a volume of  $99 \text{ \AA}^3$ , the  $c/a$  ratio and tilt angle reach the values of 1 and  $0^\circ$ , respectively, i.e., the cubic structure is obtained. From Fig. 2(b), one can also see that the tilt angle decreases more sharply starting from a volume of  $95 \text{ \AA}^3$ , but both  $c/a$  ratio and tilt angle approach their cubic limiting values in a perfectly continuous way. During the phase transition, the Rb-F bond length decreases, while at the same time the Ca-F bond length increases, and overall this produces a volume for the  $\text{CaF}_6$  octahedron that is larger in the tetragonal phase than in the cubic phase. We have been very careful to verify the absence of any jump-wise behavior in these bond lengths and the resulting tilt angle and  $c/a$  ratio by tuning numerical parameters like the number of  $\mathbf{k}$  points and the threshold for force relaxation to extreme values. In summary, all the evidence gathered from DFT supports the conclusion that the zero temperature pressure-driven phase transition  $Pm\bar{3}m \rightarrow I4/mcm$  that occurs at a negative pressure of  $P_c(T = 0 \text{ K}) = -4.8 \text{ GPa}$  mediated by octahedral tilting is of second-order. This transition is also visible when monitoring the volume dependence of the  $R_{15'}$  and  $R_{25'}$  phonon modes mentioned in Introduction. See Sec. VIII for more detailed discussions.

#### IV. ELECTRONIC PROPERTIES

The electronic properties of RbCaF<sub>3</sub> are revealed by the band structure and density of states (DOS), which are shown in Figs. 3 and 4 for the cubic and tetragonal phases, respectively, and were obtained with PBEsol and the mBJ potential.

The band structure of the cubic phase is calculated along lines connecting the high-symmetry points  $X$  (0,1/2,0),  $\Gamma$ ,  $R$  (1/2,1/2,1/2),  $M$  (1/2,1/2,0), and  $\Gamma$ , respectively. Inspection of the band structure shows that the valence band maximum is at the  $R$  point and the conduction band minimum at  $\Gamma$ , thus indicating that the fundamental band gap is indirect. The values of the fundamental band gap are shown in Table I where we can see that, as expected, all GGA methods underestimate the experimental value of 10.9 eV [46] by a large amount (more than 4 eV), while mBJ leads to a pretty good agreement with experiment since the error is significantly reduced ( $\sim 0.5 \text{ eV}$ ). Due to the strong ionicity of the system, the valence bands (covering band widths of 2 and 1.5 eV for PBEsol and mBJ, respectively) are essentially F  $2p$  states, while the unoccupied bands are mainly of Ca  $4s$ , Ca  $3d$ , and Rb  $5s$  characters to which small contributions from the Rb  $4d$  states are admixed. Compared to PBEsol, mBJ pushes the unoccupied states up. However, by looking more closely at the band structures, one can see that this shift is not rigid as it is not the same for all

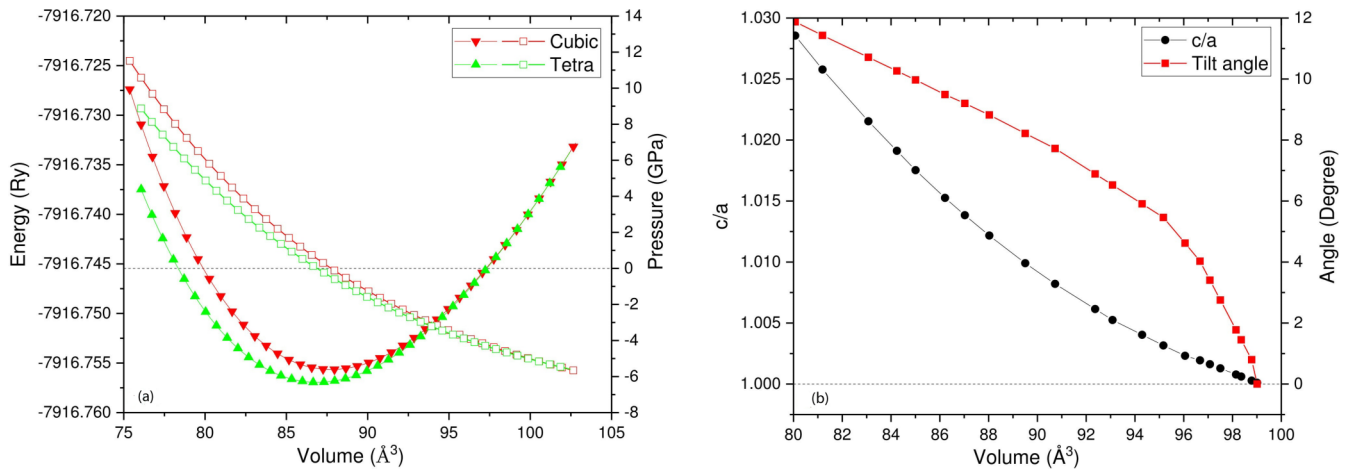


FIG. 2. (a) shows the volume dependence of the PBEsol total energy (triangles) and pressure (squares) of the cubic and tetragonal phases of RbCaF<sub>3</sub>, while (b) shows the volume dependence of the *c/a* ratio and tilt angle in the tetragonal phase. The pseudocubic cell is used for the tetragonal phase in order to compare with the cubic phase.

bands. Furthermore, the shapes of the corresponding PBEsol and mBJ bands also differ to some extent. For instance, the lowest unoccupied band at the  $\Gamma$  point is clearly narrower with the mBJ potential. In general for both the occupied and unoccupied bands, the band width is smaller with mBJ than with PBEsol or any other standard GGA.

As to the body-centered tetragonal phase, the energy band structure (left panel of Fig. 4) is calculated along lines connecting the high-symmetry points (in conventional coordinates)  $X$  ( $1/2, 1/2, 0$ ),  $\Gamma$ ,  $M$  ( $0, 0, 1$ ),  $N$  ( $1/2, 0, 1/2$ ), and  $P$  ( $1/2, 1/2, 1/2$ ), respectively. As mentioned above, the AFD

phase transition involves a doubling of the primitive unit cell and a corresponding folding of the first BZ, merging both the  $R$  and  $\Gamma$  points of the cubic BZ into the  $\Gamma$  point of the tetragonal BZ. Similarly, the  $M$  and  $X$  points of the cubic BZ merge into the  $X$  point of the BZ of the tetragonal structure. Therefore we expect the band gap in the tetragonal phase to be direct (at  $\Gamma$ ). This conjecture is indeed supported by the calculated electronic band structure which shows that both the valence band maximum and conduction band minimum are located at  $\Gamma$ . The values of the fundamental band gap, which are 6.63 and 10.58 eV with PBEsol and mBJ, respectively,

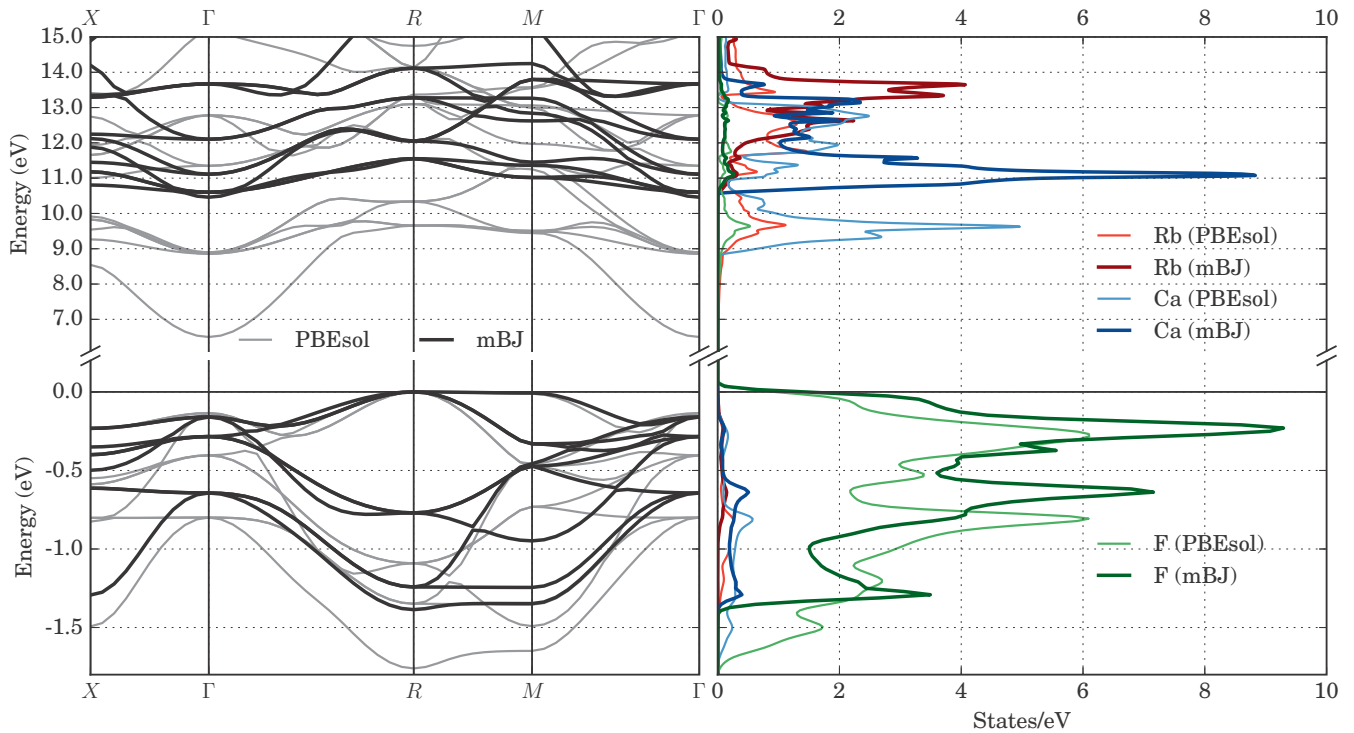


FIG. 3. Band structure (left) and DOS (right) of the cubic phase of RbCaF<sub>3</sub>. Note the different energy scales for the regions below and above the Fermi energy. The Fermi energy is set at 0.

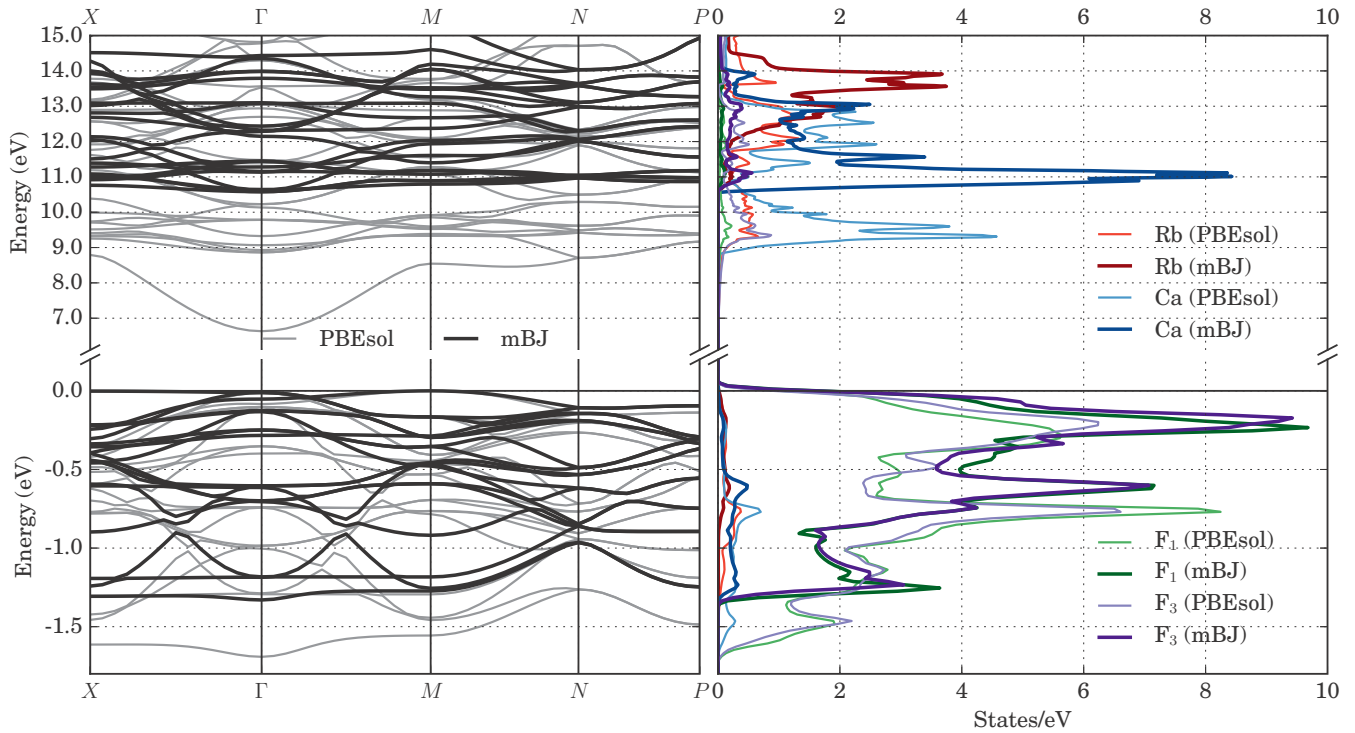


FIG. 4. Same as Fig. 3, but for the tetragonal phase.

only differ by  $\sim 0.1$  eV from the indirect band gap of the cubic phase. A comparison between the DOSs of the cubic and tetragonal phases reveals that they are essentially the same (cf. the right columns of Figs. 3 and 4).

### V. ELASTIC PROPERTIES

Generally, a crystal is mechanically stable (or at least metastable) if it is stable under both, small arbitrary inhomogeneous as well as homogeneous deformations. In terms of phonons, stability with respect to the former class of deformations is tantamount to requiring that all phonon frequencies are positive for all wave vectors throughout the BZ. The latter class of deformations can be encoded by the infinitesimal strain components  $\epsilon_i$  (written in Voigt notation with index  $i = 1, \dots, 6$ ) defined with respect to the equilibrium zero stress reference state of volume  $V_0$ . For such homogeneous deformations,

$$C_{ij}(T, V_0) = \frac{1}{V_0} \left( \frac{\partial^2 F}{\partial \epsilon_i \partial \epsilon_j} \right)_{\epsilon=0} \quad (1)$$

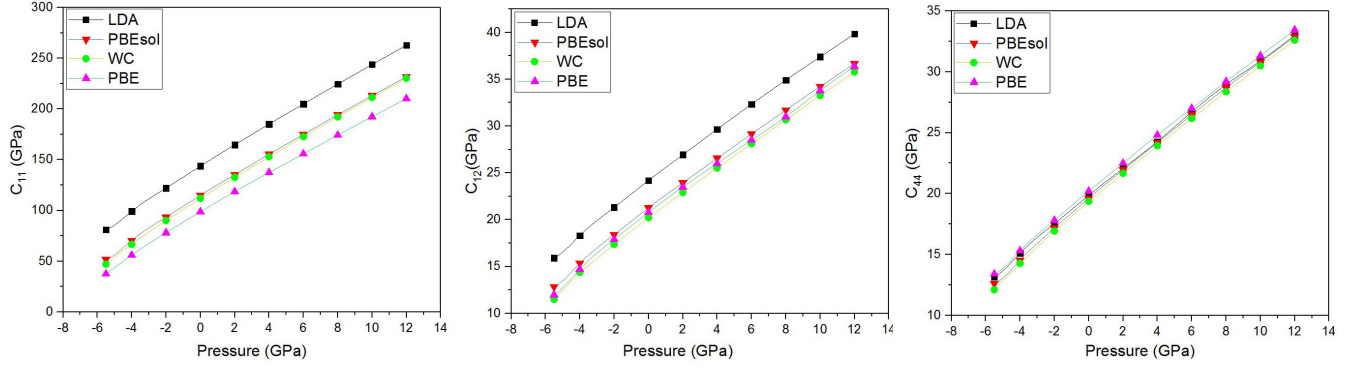
defines the  $6 \times 6$  symmetric matrices of the second-order elastic constants, where  $F$  denotes the Helmholtz free energy.

At  $T = 0$  K, where the total energy  $E$  takes over the role of the free energy  $F$ , the elastic constants can be calculated from DFT by applying to the crystal a set of deformations with respect to the equilibrium state. The deformations necessary to obtain the three independent elastic constants in cubic case ( $C_{11}$ ,  $C_{12}$ , and  $C_{44}$ ), were implemented in the ELAST program developed by Charpin [48], which is part of the WIEN2K program package.

The results for the elastic constants of  $\text{RbCa}_3\text{F}$  in the cubic phase (shown in Table III) reveal that the cubic phase satisfies the Born stability criteria [49], i.e., it is stable under homogeneous deformations. The trends among the functionals that were observed for the lattice constant and bulk modulus, namely that the PBEsol and WC result are in between those from LDA and PBE, are also reproduced with  $C_{11}$ , but not with  $C_{12}$  and  $C_{44}$ . For  $C_{12}$ , the LDA value is a bit larger than the values of other functionals. However, the differences between the various functionals are quite small in general for  $C_{44}$ . Our results agree with the previously published results (also shown in Table III) from Refs. [27,28], but not with the PBE values from Ref. [26] that resemble much more LDA values, as already observed above for the lattice constant and bulk modulus (see Sec. III). The variation of the elastic

TABLE III. Elastic constants (in GPa) of the cubic phase of  $\text{RbCaF}_3$ .

	Present work				Other works	
	LDA	PBEsol	WC	PBE	LDA	PBE
$C_{11}$	143.6	114.9	111.7	100.3	141.40 [28], 141.76 [27]	139.3 [26], 99.46 [27]
$C_{12}$	24.1	21.1	20.1	21.1	24.49 [28], 23.55 [27]	23.3 [26], 20.36 [27]
$C_{44}$	19.7	19.5	19.2	19.9	20.94 [28], 19.69 [27]	19.2 [26], 19.66 [27]

FIG. 5. Elastic constants of the cubic phase of RbCaF<sub>3</sub> as a function of pressure.

constants with respect to pressure is shown in Fig. 5, where we can see that the magnitude of all elastic constants increase rather linearly with increasing pressure. This provides a necessary input for the finite strain Landau theory [29,30] as discussed in more detail in Sec. VIII.

For the tetragonal space group  $I4/mcm$  of RbCaF<sub>3</sub> there are six independent elastic constants  $C_{11}$ ,  $C_{12}$ ,  $C_{13}$ ,  $C_{33}$ ,  $C_{44}$ , and  $C_{66}$ . The PBEsol elastic constants of the tetragonal phase were calculated with the program ELASTIC [50] and the results are shown in Table IV. From these results, we can see that the Born stability criteria [49] are satisfied. To the best of our knowledge we are not aware of any experimental or theoretical values to compare with, such that our results may act as a reference for future studies.

## VI. PHONONS

The phonon spectra were calculated using a frozen phonon approach. From the optimized structures, suitable supercells are constructed. Then, the forces, which arise due to the displacement of atoms (by 0.02 bohr), are calculated in order to form the dynamical matrix. Diagonalization of the dynamical matrix gives the phonon spectrum, where all these calculations were done by the program PHONOPY [51].

For the cubic structure, we used a  $2 \times 2 \times 2$  supercell, which consists of 40 atoms and is, according to our tests, large enough to get converged phonon spectra. On the other hand, for the two times larger body-centered tetragonal phase we used a  $2 \times 2 \times 1$  primitive supercell (80 atoms). The phonon frequencies were calculated along the  $\Gamma$ ,  $X$ ,  $M$ ,  $R$ , and  $\Gamma$  high-symmetry path of the BZ [Fig. 6(a)] of the cubic structure and along  $M$ ,  $N$ ,  $\Gamma$ ,  $X$ , and  $P$  (for the coordinates of these points see Sec. IV) for the tetragonal BZ [Fig. 6(b)], where the splitting of transverse and longitudinal optical (LO-TO) phonon modes at the  $\Gamma$  point is included using the calculated Born effective charges (BEC) (see Sec. VII).

TABLE IV. Elastic constants (in GPa) of the tetragonal phase of RbCaF<sub>3</sub> calculated with the PBEsol functional.

$C_{11}$	$C_{12}$	$C_{13}$	$C_{33}$	$C_{44}$	$C_{66}$
72	37	29	115	19	39

For the cubic phase, there are in total five modes at the  $\Gamma$  point (neglecting the LO-TO splitting), all of which are triply degenerate (see Table V). Four of them are  $T_{1u}$  modes and one is a  $T_{2u}$  mode. One of the  $T_{1u}$  modes is acoustic and the three others are IR active, while there is no Raman active mode. The  $T_{2u}$  mode, which is exclusively related to the displacement of fluorine atoms, is both IR- and Raman-silent.

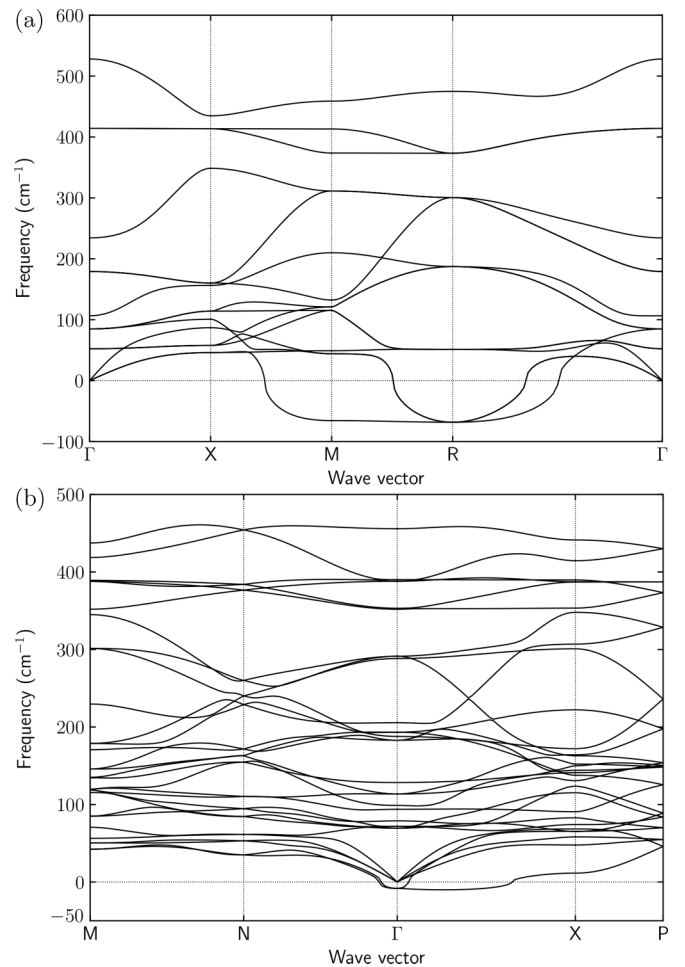


FIG. 6. (a) and (b) show the PBEsol phonon spectrum of the cubic and tetragonal phases, respectively.

TABLE V. Phonon frequencies (in  $\text{cm}^{-1}$ ) of the cubic phase of  $\text{RbCaF}_3$ . Imaginary frequencies are represented by “ $i$ ”. Frequencies obtained including LO-TO splitting at the  $\Gamma$  point are shown in parenthesis.

Modes	LDA	PBEsol	WC	PBE	Rigid-ion model [14]
$\Gamma(0, 0, 0)$					
$T_{1u}$	0	0	0	0	0
$T_{1u}$	52.5(52.5, 72.7)	50.6(50.6, 88.1)	48.5(48.5, 80.8)	55.2(55.2, 88.8)	85.3(85.3, 102.16)
$T_{2u}$	75.4(75.4, 110.6)	88.1(88.1, 104.7)	87.3(87.3, 109.1)	99.6(99.6, 112.8)	128.6
$T_{1u}$	170.1(170.1, 301.5)	179.9(179.9, 236.0)	180.0(180.0, 293.5)	187.1(187.1, 289.0)	216.4(216.4, 288.2)
$T_{1u}$	456.9(456.9, 533.0)	409.5(409.5, 524.2)	404.7(404.7, 490.8)	367.9(367.9, 460.3)	417.3(417.3, 460.7)
$R(0.5, 0.5, 0.5)$					
$R_{15'}$	77.4 <i>i</i>	64.7 <i>i</i>	64.6 <i>i</i>	46.0 <i>i</i>	21.4
$R_{25'}$	52.5	50.0	48.2	53.7	70.4
$R_{25'}$	183.9	188.5	187.7	194.3	239.9
$R_{15}$	319.5	297.2	296.2	277.0	260.4
$R_{12}$	413.0	371.2	366.1	335.2	333.8
$R_1$	507.8	474.0	469.5	446.1	443.8
$X(0, 0.5, 0)$					
$X_5$	47.1	44.0	42.5	46.1	60.1
$X_{5'}$	58.1	59.9	58.6	66.2	79.8
$X_1$	89.8	85.5	84.4	84.3	84.3
$X_{4'}$	93.9	103.2	101.5	113.5	139.2
$X_5$	108.8	116.2	115.3	124.3	150.6
$X_{2'}$	152.1	155.4	155.1	152.6	186.9
$X_{5'}$	161.9	161.1	161.3	168.2	186.6
$X_{2'}$	363.1	346.4	345.6	333.8	342.0
$X_{5'}$	456.6	409.3	404.2	367.6	415.6
$X_1$	469.6	433.1	428.4	402.5	389.8
$M(0.5, 0.5, 0)$					
$M_2$	73.7 <i>i</i>	61.9 <i>i</i>	62.14 <i>i</i>	41.7 <i>i</i>	23.4
$M_{5'}$	41.1	42.5	40.9	46.9	68.6
$M_{3'}$	49.5	45.7	44.6	48.1	59.9
$M_5$	111.5	117.5	116.5	125.5	150.2
$M_{5'}$	119.4	121.8	121.1	126.1	163.6
$M_{2'}$	127.1	132.4	132.7	135.6	132.2
$M_4$	208.7	211.2	210.3	216.2	252.7
$M_{5'}$	328.4	308.4	307.4	291.2	283.5
$M_3$	413.3	371.5	366.3	355.3	333.9
$M_{2'}$	456.2	408.8	403.8	366.8	414.1
$M_1$	492.6	457.6	453.1	428.5	418.1

At the  $R$  point, there are in total six individual modes. The triple degenerate  $R_{15}$  mode is related to the vibrations of the Ca atom, while the first of the triple degenerate  $R_{25'}$  mode is related to Rb vibrations. The remaining three modes  $R_1$ ,  $R_{12}$ , and  $R_{15'}$  have a degeneracy of one, two, and three, respectively. Of these, the  $R_{15'}$  (and also the  $M_2$ ) modes show instabilities. In particular, the instability of the  $R_{15'}$  soft mode, which corresponds to alternate rotations of the  $\text{CaF}_6$  octahedra around the cubic  $z$  axis, triggers the cubic $\rightarrow$ tetragonal phase transition.

In Table V, we present our DFT results for the phonon frequencies of the cubic phase that are compared with those derived from rigid-ion model calculations [14]. The agreement between these empirical calculations and our first-principles results is not very good and we can see that the frequencies obtained with the rigid-ion model are close to the experimentally observed frequencies in the tetragonal phase, but apparently do not correctly represent the cubic phase. As for all properties considered up to now, the phonon frequencies obtained with

PBEsol and WC are quite similar, and compared to them the values obtained with LDA and PBE show opposite trends. Typically, for higher frequency modes (mainly F vibrations), LDA obtains larger values than PBE, which is consistent with the smaller lattice constant obtained with LDA. On the other hand, for low-frequency modes, PBE leads often to larger frequencies. We have also investigated whether these shifts are due to the functional or simply due to volume effects and very different behavior can be found. For instance, for the  $T_{1u}$  mode around  $50 \text{ cm}^{-1}$  the large effect of the functional (PBE gives  $30 \text{ cm}^{-1}$  higher frequency at the LDA volume) is almost canceled by the softening due to the volume effect. On the other hand, the  $T_{2u}$  and the following  $T_{1u}$  modes show hardening with volume while the highest  $T_{1u}$  gets much softer with increasing volume, dominating the hardening effect of the PBE functional (again around  $30 \text{ cm}^{-1}$ ).

The PBEsol phonon frequencies for the tetragonal phase at the  $\Gamma$  point are presented in Table VI along with the Raman active modes measured in experiment. On lowering

TABLE VI. Phonon frequencies (in  $\text{cm}^{-1}$ ) of the tetragonal phase of  $\text{RbCaF}_3$  at the  $\Gamma$  point calculated with the PBEsol functional are compared with experimental values obtained by Raman spectrum [14]. Nonobserved Raman modes and imaginary frequencies are denoted with “n.o.” and “ $i$ ” respectively.

Modes	Present	Expt. (15 K)	Expt. (50 K)	Expt. (80 K)
$E_g$	5.1 <i>i</i>	n.o	23	22.5
$A_{2u}$	0			
$E_u$	0			
$E_u$	69.6			
$E_g$	71.9	74	75	75
$B_{2g}$	78.9	87.7	83	n.o
$A_{2u}$	93.9			
$A_{1g}$	98.0	82	81	80
$E_u$	113.5			
$B_{1u}$	128.5			
$E_u$	182.8			
$A_{2u}$	187.9			
$E_g$	193.4	202	200	201
$B_{2g}$	205.4	210	210	211
$A_{1u}$	288.8			
$E_u$	291.4			
$B_{1g}$	352.1	364	364	365
$A_{2g}$	353.7			
$E_u$	388.4			
$A_{2u}$	391.0			
$A_{2g}$	456.1			

the symmetry from cubic to tetragonal, the degeneracies of the cubic phonon modes are partly lifted, which is reflected in the observed spectra of the tetragonal modes. Similarly as for the electronic band structure discussed in Sec. IV, the tetragonal  $\Gamma$  point hosts modes derived by back-folding from the  $\Gamma$  and  $R$  points of the parent cubic phase, while the tetragonal  $X$  point modes are inherited from the cubic  $X$  and  $M$  point modes. At the tetragonal  $\Gamma$  point, eight IR active modes ( $3A_{2u}$ ,  $5E_u$ ), seven Raman active modes ( $A_{1g}$ ,  $B_{1g}$ ,  $2B_{2g}$ ,  $3E_g$ ), and four silent modes ( $A_{1u}$ ,  $B_{1u}$ ,  $2A_{2g}$ ) are identified, leaving the remaining acoustic modes  $A_{2u}$ ,  $E_u$ . The comparison with experiment shows that PBEsol leads to good agreement with experiment. The largest discrepancy is for the  $A_{1g}$  mode, which is overestimated by  $16 \text{ cm}^{-1}$ . All experimentally observable modes originate originally from cubic  $R$ -point phonons. The softest  $E_g$  and the  $A_{1g}$  modes originate from the unstable cubic  $R_{15'}$  mode while the two pairs of  $E_g$  and  $B_{2g}$  modes are hardened by  $5\text{--}28 \text{ cm}^{-1}$  compared to the cubic  $R_{25'}$  modes. Finally, the observed  $B_{1g}$  mode is softer by nearly  $20 \text{ cm}^{-1}$  than its corresponding  $R_{12}$  mode.

Figure 6, which presents the phonon spectrum in both phases, indicates that the tetragonal structure is more stable than the cubic one, but still shows a slight instability of its  $E_g$  mode. In order to understand these observations, one should bear in mind that our DFT calculations at  $T = 0 \text{ K}$  do not account for the entropic effects that are present at nonzero temperature. From experiment, it has been found that the cubic structure only stabilizes above temperature of about  $200 \text{ K}$ , while the tetragonal structure, being a low-temperature

descendant of its cubic parent, is stable within the temperature range  $50\text{--}200 \text{ K}$ . The lowest temperature phase found below  $20 \text{ K}$  is orthorhombic as described in Ref. [52] and the residual  $E_g$  mode instability in the tetragonal phase should be due to the orthorhombic distortion, which was not investigated in this paper.

## VII. BORN EFFECTIVE CHARGES

In order to quantitatively understand the splitting between transverse and longitudinal optical phonon modes, we calculated the Born effective charges. The BEC tensor  $Z^*$ , which was introduced by Born [53], is a dynamic quantity capturing the effects of the long-range Coulomb interaction. Formally, it is derived from the change in polarization  $\mathbf{P}$  with respect to a displacement of an ion [54]:

$$Z_{v,\alpha\beta}^* = \frac{\Omega_0}{|e|} \frac{\partial \mathbf{P}_\beta}{\partial \mathbf{r}_{v,\alpha}}, \quad (2)$$

where  $\Omega_0$  is the unit cell volume and  $\partial \mathbf{P}_\beta$  is the change in polarization in direction  $\beta$  due to the small displacement  $\partial \mathbf{r}_{v,\alpha}$  of the atom  $v$  in the direction  $\alpha$  from its equilibrium position. Using the software package BERRYPI [55], which is included in WIEN2K, we can compute the polarization in  $\text{RbCaF}_3$ .

In the cubic structure, the Born effective charge tensors for the Rb and Ca atoms are isotropic for site symmetry group  $O_h$ . For the F atom, the site symmetry group is  $D_{4h}$  and the two independent components  $F_{\parallel}$  and  $F_{\perp}$ , corresponding to displacements of F parallel and perpendicular to the Ca-F bond, differ by more than 50%. From Table VII, it becomes also clear that different DFT functionals in the cubic phase show the same kind of behavior seen in other properties. The BEC values obtained by PBEsol and WC are in between the result obtained by LDA and PBE. We have verified that LDA gives the highest BEC because it has the smallest equilibrium lattice constant (for the same volume the differences between LDA and PBE are well below 0.01), but overall the variations with the different functionals are rather small. As usual, the BEC are a bit larger than the formal ionic charges and are in particular much larger than what was used in the rigid ion phonon calculations in Ref. [14].

In the tetragonal phase, the BEC tensor  $Z^*$  of Rb and Ca have two distinct values, whereas F atoms (F1 and F3) have three distinct values (Table VII), since there are considerable atomic displacements involved in the transformation from the cubic to tetragonal structure for the F atom. Nevertheless, we observe that the values of the BEC remain relatively close to their nominal ionic charges, a behavior that is similar to what is also exhibited by other fluoroperovskites but opposite to that of oxygen perovskites [54,56,57]. Strongly anomalous BEC play an important role in explaining ferroelectricity in perovskite oxides. Its absence, in turn, hints to a nonferroelectricity of fluoro-perovskites in most cases. A similar behavior has also been reported in other fluoroperovskites (see Ref. [58]). However, there are also some exceptions like in the case of the high-temperature ferroelectricity that is observed in  $\text{CsPbF}_3$  [6].

When comparing the values of the BEC in both phases for PBEsol, we find that  $Z^*(\text{Ca})$  remains almost unchanged but there is a slight asymmetry of about 4% in  $Z^*(\text{Rb})$ . There



TABLE VII. Born effective charges ( $Z^*$ ) of Rb, Ca, and F calculated with different functionals in the cubic phase and with PBEsol in the tetragonal phase.  $F_{\parallel}$  and  $F_{\perp}$  indicate the Born effective charge of the F atom when it is displaced parallel or perpendicular to the Ca-F bond, respectively.

	Nominal	Cubic				Tetragonal	
		LDA	WC	PBEsol	PBE	PBEsol	
$Z^*(\text{Rb})$	1	1.23	1.23	1.22	1.21	1.20 <sub>[100]</sub>	
	1	1.23	1.23	1.22	1.21	1.20 <sub>[010]</sub>	
	1	1.23	1.23	1.22	1.21	1.27 <sub>[001]</sub>	
$Z^*(\text{Ca})$	2	2.37	2.35	2.35	2.34	2.36 <sub>[100]</sub>	
	2	2.37	2.35	2.35	2.34	2.36 <sub>[010]</sub>	
	2	2.37	2.35	2.35	2.34	2.35 <sub>[001]</sub>	
$Z^*(F_{\parallel})$	-1	-1.66	-1.64	-1.64	-1.63	-1.64(F1)	-1.60(F3)
$Z^*(F_{\perp})$	-1	-0.97	-0.97	-0.97	-0.96	-0.97(F1)	-0.97(F3)
	-1	-0.97	-0.97	-0.97	-0.96	-0.96(F1)	-1.00(F3)

are two inequivalent F atoms in the tetragonal phase.  $Z^*(F1)$  remains almost the same as in the cubic structure, but for  $Z^*(F3)$  an increased asymmetry of about 2.4% compared to the cubic values can be seen and in addition the  $x$  and  $y$  directions become slightly different due to the rotation of the F octahedra.

### VIII. PRESSURE-DRIVEN PHASE TRANSITION

Figure 7 shows the volume dependence of the  $R_{15'}$  and  $R_{25'}$  phonon modes with three different functionals (WC is similar to PBEsol and therefore not shown). Gradually increasing the volume of the unit cell (thus lowering the pressure), the  $R_{15'}$  mode is found to harden and to become positive at about  $99 \text{ \AA}^3$ , which is in agreement with the observations made above for the  $c/a$  ratio and the tilt angle of the  $\text{CaF}_6$  octahedron that approach 1 and 0 at this volume, respectively. Altogether, this once more indicates that a tetragonal  $\rightarrow$  cubic pressure-driven transition does occur at a negative pressure

of  $-4.8 \text{ GPa}$ . In the vicinity of the transition volume, the curves for the  $R_{15'}$  and  $R_{25'}$  modes sharply increase and decrease, respectively. Figure 7 also shows that the  $R_{15'}$  mode is more or less insensitive to the functional, as observed in  $\text{SrTiO}_3$ , [59] whereas the  $R_{25'}$  phonon mode shows a much more pronounced dependence and becomes unstable at much larger volumes except for LDA, where both modes would be unstable in a volume range of  $91\text{--}98 \text{ \AA}^3$ .

In the field of structural phase transitions, it has been standard practice for many decades to analyze phase transitions of the group-subgroup type using the machinery of Landau theory (LT) [60,61], which provides a convenient unifying framework for all important thermodynamic and crystallographic aspects. From the perspective of LT, it is however rather puzzling to reconcile our observation of the second-order nature of the  $P$ -driven transition at  $T = 0 \text{ K}$  with the above mentioned experimental findings of a weakly first-order thermal transition between 193 and 199 K at ambient pressure and the detection of clear signs of a first-order high-pressure transition at  $P_c(300 \text{ K}) = 2.8 \text{ GPa}$  for ambient temperature in Ref. [23]. In fact, as discussed at length in Ref. [30], it is virtually impossible to explain such a change from first to second order within the framework of traditional LT. In the present paper, however, we do not intend to duplicate the corresponding discussion. Moreover, for  $\text{RbCaF}_3$ , no complete set of Landau parameters seems to be available in the literature, such that our present discussion must remain at the qualitative level anyway. In a nutshell, however, we would like to offer the following explanation.

Recall that a standard Landau free energy expansion [60,61] is a polynomial expansion in powers of the components of a primary order parameter and possibly additional secondary order parameter(s). Reflecting the three possible choices for the octahedral rotation axis, the primary order parameter  $Q$  of the cubic-tetragonal transition, whose modulus is proportional to the octahedral tilt rotation angle  $\phi$ , has three components ( $Q_1, Q_2, Q_3$ ). To incorporate elastic response, we consider the infinitesimal strains  $\epsilon_i, i = 1, \dots, 6$  as secondary order parameter components. The key requirement for a Landau free energy expansion is its order-by-order invariance under the action of space group of the high-symmetry phase, which in the present case is the cubic group

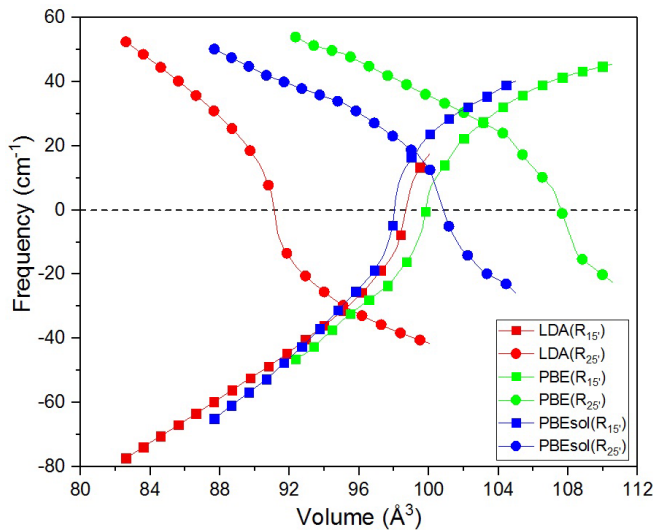


FIG. 7. Volume dependence of the  $R_{15'}$  and  $R_{25'}$  phonon modes of the cubic phase of  $\text{RbCaF}_3$ . Imaginary frequencies are represented by negative numbers.

$Pm\bar{3}m$ . A free energy expansion exclusively built from the corresponding cubic invariants up to sixth order yields

$$F_q = \frac{A(T)}{2}(Q_1^2 + Q_2^2 + Q_3^2) + \frac{b_1}{4}(Q_1^2 + Q_2^2 + Q_3^2)^2 + \frac{b_2}{4}(Q_1^4 + Q_2^4 + Q_3^4) + \frac{c}{6}(Q_1^2 + Q_2^2 + Q_3^2)^3 + \frac{c'}{6}(Q_1 Q_2 Q_3)^2 + \frac{c''}{6}(Q_1^2 + Q_2^2 + Q_3^2) \times (Q_1^4 + Q_2^4 + Q_3^4). \quad (3)$$

Introducing the so-called symmetry-adapted strains [62]

$$\epsilon_a = \epsilon_1 + \epsilon_2 + \epsilon_3, \quad (4a)$$

$$\epsilon_o = \epsilon_1 - \epsilon_2, \quad (4b)$$

$$\epsilon_t = (2\epsilon_3 - \epsilon_1 - \epsilon_2)/\sqrt{3} \quad (4c)$$

allows to decompose the harmonic cubic elastic free energy  $F_{el} = \sum_{ij}(C_{ij}^0/2)\epsilon_i\epsilon_j$  into [62]

$$F_{el} = \frac{K_0}{2}\epsilon_a^2 + \frac{\mu_0}{2}(\epsilon_o^2 + \epsilon_t^2) + \frac{C_{44}^0}{2}(\epsilon_4^2 + \epsilon_5^2 + \epsilon_6^2), \quad (5)$$

where  $K_0 = (C_{11}^0 + 2C_{12}^0)/3$  and  $\mu_0 = (C_{11}^0 - C_{12}^0)/2$  denote the cubic bulk and longitudinal shear moduli, respectively, and the subscript or superscript “0” are used to label the harmonic elastic moduli of the cubic reference phase. As to the allowed couplings between primary order parameter and strain, up to linear order in strain and quadratic order in  $Q_i$ , we list

$$F_c = \lambda_1\epsilon_a(Q_1^2 + Q_2^2 + Q_3^2) + \lambda_2[\sqrt{3}\epsilon_o(Q_2^2 - Q_3^2) + \epsilon_t(2Q_1^2 - Q_2^2 - Q_3^2)] + \lambda_3(\epsilon_6 Q_1 Q_2 + \epsilon_5 Q_1 Q_3 + \epsilon_4 Q_2 Q_3). \quad (6)$$

The thermodynamic behavior of the coupled system of order parameter and strain components is therefore—at least for small strains and in the vicinity of  $T_c$ —approximately governed by the Landau free energy

$$F = F_q + F_{el} + F_c. \quad (7)$$

In accordance with the usual assumptions of LT, we expect

$$A(T) \approx A_0(T - T_0) \quad (8)$$

to depend roughly linearly on temperature, while a possible  $T$  dependence of all other coupling coefficients appearing in the potentials (3), (5), and (6) is neglected.

In the tetragonal phase  $\eta \equiv Q_1, Q_2 = Q_3 = 0$ , we have

$$F_q = \frac{A(T)}{2}\eta^2 + \frac{B}{4}\eta^4 + \frac{C}{6}\eta^6, \quad (9a)$$

$$F_c = \lambda_1\epsilon_a\eta^2 + 2\lambda_2\epsilon_t\eta^2, \quad (9b)$$

where  $B \equiv b_1 + b_2$  and  $C \equiv c + c''$ . From the hydrostatic pressure conditions  $\frac{\partial F}{\partial \epsilon_a}|_{\epsilon_a=\bar{\epsilon}_a} = -P$  and  $\frac{\partial F}{\partial \epsilon_t}|_{\epsilon_t=\bar{\epsilon}_t} = 0$ , we determine the spontaneous stresses  $\bar{\epsilon}_a = -\frac{\lambda_1\eta^2 + P}{K_0}$  and  $\bar{\epsilon}_t = -\frac{2\lambda_2\eta^2}{\mu_0}$ , which are used to replace strain by pressure dependence by virtue of a Legendre transform  $F \rightarrow G$ . The

resulting Gibbs free energy  $G$  turns out to be

$$G = F_q - \frac{\lambda_1 P}{K_0}\eta^2 - \left(\frac{\lambda_1^2}{2K_0} + \frac{2\lambda_2^2}{\mu_0}\right)\eta^4 - \frac{P^2}{2K_0} \equiv \frac{A(T, P)}{2}\eta^2 + \frac{\tilde{B}}{4}\eta^4 + \frac{C}{6}\eta^6 - \frac{P^2}{2K_0}. \quad (10)$$

Thus, for hydrostatic pressure, the strain coupling effects could be completely absorbed in a renormalized  $P$ -dependent scalar order parameter potential with a linearly  $P$ -dependent quadratic coefficient

$$A(T, P) = A(T) - \frac{2\lambda_1 P}{K_0} \quad (11)$$

and a *reduced but  $P$ -independent* quartic coefficient

$$\tilde{B} = B - \frac{2\lambda_1^2}{K_0} - \frac{8\lambda_2^2}{\mu_0}. \quad (12)$$

This negative shift, which involves the ratio of the strain-order parameter coupling coefficient(s) to the “bare” harmonic elastic constants, may or may not produce a negative sign of the resulting effective fourth order coupling coefficient  $\tilde{B}$ . While the parameter  $C$  is assumed to be constant and positive for obvious stability reasons, the physically important parameters that govern the physics of the phase transition captured by the effective single domain Landau potential (10) are the quadratic parameter  $A(T, P)$  and the quartic parameter  $\tilde{B}$ . All other parameters remaining inert. In this effective LT the transition is triggered by the evolution of the quadratic parameter  $A(T, P)$ . In fact, it is easy to see Refs. [60,61] that for  $\tilde{B} \geq 0$ , we find a line of second-order transition points  $(T, P_c(T))$  given by  $A(T, P_c(T)) \equiv 0$ , while for  $\tilde{B} < 0$ , a first-order phase boundary  $(T, P_c(T))$  is predicted, which is determined by the equation  $A(T, P_c(T)) \equiv \frac{3\tilde{B}^2}{16C}$ . Comparing the critical pressure  $P_c(T)$  at an arbitrary temperature  $T$  to that at room temperature  $T = T_R$ , the condition  $A(T_R, P_c(T_R)) \equiv A(T, P_c(T))$ , which holds both for the first- and second-order cases, yields the linear relation

$$P_c(T) = P_c(T_R) + \frac{K_0}{2\lambda_1}A_0(T - T_R). \quad (13)$$

The crucial parameter determining the so-called *Clapeyron slope*  $dP_c(T)/dT = \frac{K_0}{2\lambda_1}A_0$  of the resulting linear phase border is the Landau coupling parameter  $\lambda_1$ . If it is positive,  $P_c(T)$  decreases on lowering the temperature. For example, in the case of SrTiO<sub>3</sub> and KMnF<sub>3</sub>, room temperature AFD transitions  $Pm\bar{3}m \rightarrow I4/mcm$  completely similar to our present case are detected at 9.6 [63] and 3.4 GPa [64], whereas they occur at  $T = 105$  [65] and 185.6 K [66], respectively, under ambient pressure conditions. For RbCaF<sub>3</sub>, our present DFT calculations yield  $P_c(T = 0) = -4.8$  GPa, while the pressure driven cubic-to-tetragonal phase transition is experimentally observed at a positive pressure of 2.8 GPa at room temperature in Ref. [23]. These facts are also consistent with a positive value  $\lambda_1 > 0$ , which was to be expected given the similarity of all these transitions. As an example for a negative Clapeyron slope, i.e.,  $\lambda_1 < 0$ , we mention the ferroelectric-to-paraelectric phase transition in PbTiO<sub>3</sub>. Under ambient pressure it occurs at  $T_c \approx 492^\circ\text{C}$ , while at room temperature it takes  $P_c = 12$  GPa to observe it [30].

However, the LT prediction (12) of a  $P$ -independent reduced quartic coefficient  $\tilde{B}$  is fundamentally inconsistent with the available information extracted from DFT versus experiment. As emphasized above, the sign of  $\tilde{B}$  determines the order of the transition, which is predicted to be of second order for  $\tilde{B} > 0$  and first order for  $\tilde{B} < 0$ . The manifest  $P$ -independence of (12) therefore implies that by changing  $P$  it should not be possible to convert the transition from first to second order. For RbCaF<sub>3</sub>, however, we unambiguously observe a second-order transition at negative pressure, indicating  $\tilde{B} > 0$ , while a first-order one at positive  $P$  is seen at room temperature and positive pressure, which is only possible for  $\tilde{B} < 0$ . Traditional LT is thus unable to offer any convincing mechanism explaining this apparent change of character. In this respect, however, RbCaF<sub>3</sub> is certainly not an isolated incident. In fact, the above mentioned ferroelectric transition in PbTiO<sub>3</sub> is of pronounced first-order character at ambient pressure, while at 12 GPa, it appears to be of second-order within experimental resolution. In KMnF<sub>3</sub>, the ambient temperature high-pressure transition is weakly first-order, but the ambient pressure transition is second-order. So what is wrong with the conventional Landau description?

In the traditional approach, the elastic energy expansion is truncated beyond harmonic order. Implicitly, this forces all cubic elastic moduli entering in this expansion to be independent of pressure. A glance at Fig. 5, where the calculated pressure dependence of cubic elastic constants of RbCaF<sub>3</sub> is shown, demonstrates that the harmonic approximation breaks down. In fact, within the relevant pressure range  $C_{11}^0$  changes from  $C_{11}^0(-4.8 \text{ GPa}) \approx 50 \text{ GPa}$  to some  $C_{11}^0(2.8 \text{ GPa}) \approx 130 \text{ GPa}$ , and similarly  $C_{12}^0(-4.8 \text{ GPa}) \approx 15 \text{ GPa}$  to  $C_{12}^0(2.8 \text{ GPa}) \approx 25 \text{ GPa}$ . This behavior is impossible to reconcile with a simple harmonic elastic energy approach. It has already been recognized in Ref. [67] that a nonlinear and anharmonic extension of Landau theory coupled to finite strain is required once the external pressure becomes non-negligible in comparison to the elastic constants. It is only rather recently [29,30,68–70] that such a nontrivial extension of LT has been constructed. Not unexpectedly, its backbone is the mathematically consistent incorporation of the pressure-dependence of elastic constants. Even without knowledge of all technical details, one may immediately anticipate that such theory should be capable of explaining the observed change of the nature of the transition from first to second order. Once  $K_0$  and  $\mu_0$  were formally allowed to depend on  $P$ , Eq. (12) would suggest that  $\tilde{B}$  should inherit a nontrivial  $P$  dependence.

For some of the mentioned examples, this new approach has already been worked out quantitatively and indeed proves to be able to theoretically explain the change from first to second-order character observed in experiment. In Ref. [30], the quartic parameter  $B(T, P) \approx B(P)$  of PbTiO<sub>3</sub> is found to start out negative at ambient pressure but with a positive pressure slope, and for  $P \gtrsim 0.5 \text{ GPa}$  becomes positive. A related behavior was also observed [29] in an application to the AFD transition of SrTiO<sub>3</sub>, where the quartic coefficient starts out positive but with negative pressure slope, and is observed to change sign in the vicinity of the ambient temperature transition pressure  $P_c = 9.6 \text{ GPa}$ .

Unfortunately, for RbCaF<sub>3</sub>, a complete numerical parametrization of the underlying Landau potential remains

to be worked out, such that we must content ourselves with a qualitative discussion, in which we shall rely on the close similarity of the transition to the one in SrTiO<sub>3</sub>. Thus let us assume that the quartic effective Landau parameter for RbCaF<sub>3</sub> also decreases roughly linearly with  $P$ . As mentioned before, experimentally the ambient pressure thermal transition of RbCaF<sub>3</sub> at 193–197 K was found to be of weakly first-order, which would translate into an ambient pressure quartic Landau parameter that is slightly negative. Based on this information and assuming a behavior similar to that of SrTiO<sub>3</sub>, one would therefore anticipate that the corresponding ambient temperature high-pressure phase transition, which takes place at 2.8 GPa should definitely be of first-order with a much more pronounced first-order character, which is exactly what is found in experiment (Ref. [23]). On the other hand, assuming the roughly linear increase of the quartic Landau coupling with falling pressure, its value at  $-4.8 \text{ GPa}$  is very likely to be positive, which translates into the second-order behavior we have detected in our present simulations.

The preceding theoretical discussion of LT has shown that switching from a strain—to a pressure—parametrized description by virtue of the Legendre transformation (10) resulted in a much simpler and more transparent formalism which provided additional physical insight. This suggests to parametrize our DFT results in terms of  $P$  rather than  $V$  as well. Mathematically, one passes from energies  $E(V)$  to enthalpies  $H(P) = E(V(P)) + PV(P)$ . While this may seem in principle straightforward, numerically, the resulting enthalpies  $H_{\text{cubic}}$  and  $H_{\text{tetra}}$  of both phases usually differ only in the mRy range. Thus our DFT calculation of the enthalpy difference  $\Delta H = H_{\text{cubic}} - H_{\text{tetra}}$  of both phases, which is displayed in the upper panel of Fig. 8, required a careful control of tiny energy offsets arising from the use of (necessarily finite and incommensurate) fast Fourier grids or  $k$  meshes, which are rotated by 45° relative to each other in the corresponding cells.

For the  $P$  dependence of the other observables of the pressure-driven transition, we find that  $c/a$  is indeed linear in  $P - P_c$  in accordance with LT (cf. middle panel of Fig. 8). Interestingly, we observe that the tilt angle  $\phi$ , which represents the order parameter of the transition, does not follow the classical Landau prediction  $\phi \sim \sqrt{P - P_c}$ , but rather seems to obey a power law  $\phi \sim (P - P_c)^{\beta_P}$  governed by an exponent of  $\beta_P \approx 0.36$ . This is remarkable for the following reasons. As we have mentioned above, from the point of view of symmetry, the soft mode behavior of the AFD transition of RbCaF<sub>3</sub> is similar to that of the well-studied 105 K transition in SrTiO<sub>3</sub>. As to its critical behavior, an early renormalization group analysis by Cowley and Bruce [71] shows that this transition should belong to the universality class of the three-dimensional (3D) antiferromagnetic Heisenberg model. The static critical indices should thus coincide with those of the classical ferromagnetic Heisenberg model [72]. In the present context, it may be objected that we are actually dealing with a compressible version of the 3D Heisenberg model with  $P$  rather than  $T$  driving the transition. Integrating out the infinitesimal strains from a corresponding order-parameter and strain dependent effective Hamiltonian, the bare quadratic term of the resulting purely order-parameter dependent

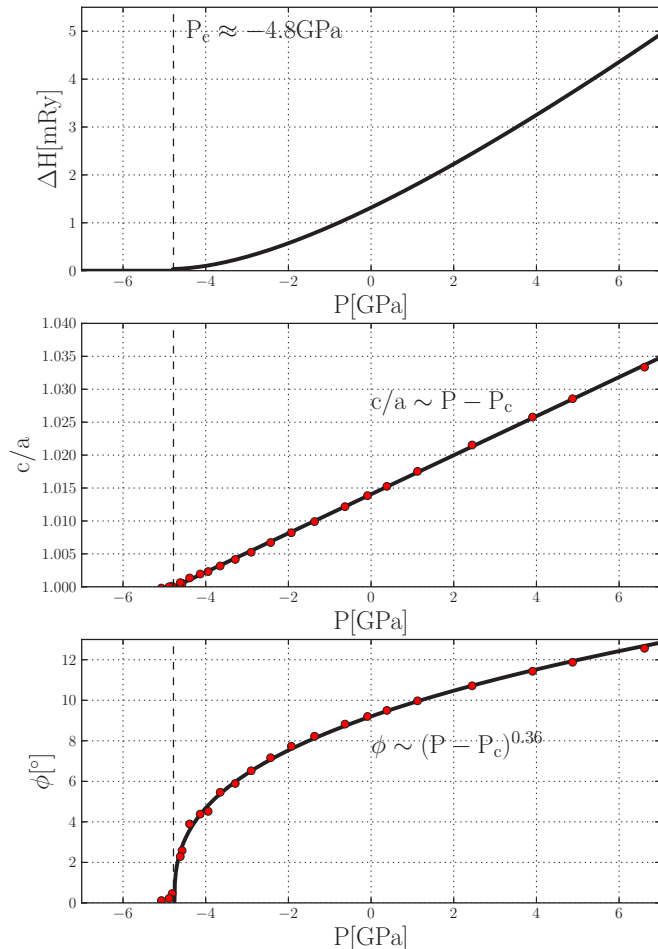


FIG. 8. From top to bottom; the behavior of enthalpy difference  $\Delta H = H_{\text{cubic}} - H_{\text{tetra}}$  between cubic and tetragonal phase, tilt angle, and  $c/a$  ratio is shown with respect to pressure.

effective Hamiltonian does acquire a linear  $P$  dependence similar to that on temperature [73]. We would therefore anticipate that  $\beta_P$  should coincide with the exponent  $\beta$  which governs the power-law behavior  $\phi(\tau) \sim |\tau|^\beta$  of the order parameter as a function of reduced temperature  $\tau = (T - T_c)/T_c$ . In Ref. [74], these exponents have been determined by state-of-the-art Monte Carlo methods, and the resulting value of  $\beta$  for the 3D Heisenberg model is  $\beta = 0.3689(3)$ .

While this apparent numerical agreement between exponents  $\beta_P$  and  $\beta$  is certainly remarkable, it may be too good to be true for several reasons. Theoretically, integrating out the strains also produces a nonlocal fourth-order coupling in the remaining effective lattice spin Hamiltonian, and this generally induces a fluctuation-induced first-order transition [75,76] instead of a second-order one, which may, however, be very difficult to detect due to its weak character. At a more

practical level, it is hard to believe that we should actually have observed true critical behavior. DFT is essentially a mean-field method based on homogeneous configurations, while criticality implies long-range spatial correlations. Instead, the observed power-law behavior may very well be merely “pseudocritical” and might be reproducible within LT by taking into account the effects of sixth or possible higher powers of the order parameter, but that still remains to be shown. In addition, any such explanation must also simultaneously reproduce the linear increase of  $c/a$  with  $P$ , which, according to classical LT should be proportional to the tetragonal strain  $\bar{\epsilon}_t$  and thus to the square of the order parameter, which is obviously at odds with the observed power law and  $\beta_P \neq 1/2$ .

In any case, for  $\text{RbCaF}_3$ , all these questions are somewhat academic, since the tetragonal phase is not the  $T = 0$  K ground state and therefore the aforementioned power law in  $P - P_c$  will never be observable in experiment. But this may be different for other perovskites,  $\text{SrTiO}_3$  certainly being an interesting candidate for a corresponding investigation.

## IX. SUMMARY AND CONCLUSION

In this paper, we calculated the electronic, structural, and vibrational properties of  $\text{RbCaF}_3$  in its cubic and tetragonal phases. The analysis of phonon spectra indicates that the observed AFD phase transition is caused by the softening of an  $R_{15}$  mode. This is in complete agreement with the previous experimental studies [14]. The electronic band gap changes from indirect to direct as due to back-folding of the cubic BZ into the tetragonal one. We also observe the presence of weakly anomalous Born effective charges, which play an important role in explaining the absence of ferroelectricity in  $\text{RbCaF}_3$ . A similar behavior is also observed in other fluoroperovskites [58]. In the framework of finite strain Landau theory, the observed change in the character of the pressure-induced transition from second order at zero temperature to first order at ambient temperature can be understood by postulating a linear decrease of the quartic Landau coupling parameter with increasing pressure. However, it remains to work out a complete numerical parametrization for the underlying Landau potential of  $\text{RbCaF}_3$ . This would be even more desirable in order to further study the alleged pseudocritical power-law behavior demonstrated in Sec. VIII.

## ACKNOWLEDGMENTS

We would like to thank W. Schranz for valuable discussions. S.E. and P.B. acknowledge financial support from Higher Education Commission (HEC), Pakistan. A.T. acknowledges support by the Austrian Science Fund (FWF) Project P27738-N28. F.T. and P.B. acknowledge support by the FWF Project F41 (SFB ViCoM).

- [1] J. Huang, Y. Yuan, Y. Shao, and Y. Yan, *Nat. Rev. Mater.* **2**, 17042 (2017).  
 [2] N.-G. Park, M. Grätzel, T. Miyasaka, K. Zhu, and K. Emery, *Nat. Energy* **1**, 16152 (2016).

- [3] G. Hörsch and H. J. Paus, *Opt. Commun.* **60**, 69 (1986).  
 [4] R. Hua, B. Lei, D. Xie, and C. Shi, *J. Solid State Chem.* **175**, 284 (2003).

- [5] K. Shimamura, H. Sato, A. Bensalah, V. Sudesh, H. Machida, N. Sarukura, and T. Fukuda, *Cryst. Res. Technol.* **36**, 801 (2001).
- [6] P. Berastegui, S. Hull, and S.-G. Eriksson, *J. Phys.: Condens. Matter* **13**, 5077 (2001).
- [7] T. Nishimatsu, N. Terakubo, H. Mizuseki, Y. Kawazoe, D. Pawlak, K. Shimamura, and T. Fukuda, *Jpn. J. Appl. Phys.* **41**, L365 (2002).
- [8] H. Megaw, *Crystal Structures* (W.B. Saunders, London, 1973).
- [9] A. M. Glazer, *Acta Crystallogr., Sect. A: Cryst. Phys., Diff., Theor. Gen. Crystallogr.* **31**, 756 (1975).
- [10] T. Riste, E. Samuelsen, K. Otnes, and J. Feder, *Solid State Commun.* **9**, 1455 (1971).
- [11] R. A. Evarestov, E. Blokhin, D. Gryaznov, E. A. Kotomin, and J. Maier, *Phys. Rev. B* **83**, 134108 (2011).
- [12] G. Shirane, V. Minkiewicz, and A. Linz, *Solid State Commun.* **8**, 1941 (1970).
- [13] N. Sai and D. Vanderbilt, *Phys. Rev. B* **62**, 13942 (2000).
- [14] P. Daniel, M. Rousseau, and J. Toulouse, *Phys. Rev. B* **55**, 6222 (1997).
- [15] A. Rushworth and J. Ryan, *Solid State Commun.* **18**, 1239 (1976).
- [16] A. Bulou, C. Ridou, M. Rousseau, J. Nouet, and A. Hewat, *J. Phys. France* **41**, 87 (1980).
- [17] T. W. Ryan, R. J. Nelmes, R. A. Cowley, and A. Gibaud, *Phys. Rev. Lett.* **56**, 2704 (1986).
- [18] A. Gibaud, T. W. Ryan, and R. J. Nelmes, *J. Phys. C* **20**, 3833 (1987).
- [19] A. Gibaud, R. A. Cowley, and P. W. Mitchell, *J. Phys. C* **20**, 3849 (1987).
- [20] J. C. Ho and W. P. Unruh, *Phys. Rev. B* **13**, 447 (1976).
- [21] M. Rousseau, J. Nouet, and R. Almairac, *J. Phys. France* **38**, 1423 (1977).
- [22] R. Almairac, M. Rousseau, J. Y. Gesland, J. Nouet, and B. Hennion, *J. Phys. France* **38**, 1429 (1977).
- [23] K. S. Knight, W. G. Marshall, and P. M. Hawkins, *Phys. Chem. Miner.* **41**, 461 (2014).
- [24] J. J. Martin, G. S. Dixon, and P. P. Velasco, *Phys. Rev. B* **14**, 2609 (1976).
- [25] G. Murtaza, I. Ahmad, and A. Afaq, *Solid State Sci.* **16**, 152 (2013).
- [26] B. Ghebouli, M. Fatmi, M. Ghebouli, H. Choutri, L. Louail, T. Chih, A. Bouhemadou, and S. Bin-Omran, *Solid State Sci.* **43**, 9 (2015).
- [27] L. Li, Y.-J. Wang, D.-X. Liu, C.-G. Ma, M. G. Brik, A. Suchocki, M. Piasecki, and A. H. Reshak, *Mat. Chem. Phys.* **188**, 39 (2017).
- [28] K. E. Babu, N. Murali, K. V. Babu, B. K. Babu, and V. Veeraiyah, *AIP Conf. Proc.* **1661**, 100002 (2015).
- [29] A. Tröster, W. Schranz, F. Karsai, and P. Blaha, *Phys. Rev. X* **4**, 031010 (2014).
- [30] A. Tröster, S. Ehsan, K. Belbase, P. Blaha, J. Kreisel, and W. Schranz, *Phys. Rev. B* **95**, 064111 (2017).
- [31] P. Blaha, K. Schwarz, G. K. H. Madsen, D. Kvasnicka, J. Luitz, R. Laskowski, F. Tran, and L. D. Marks, *WIEN2K: An Augmented Plane Wave plus Local Orbitals Program for Calculating Crystal Properties* (Vienna University of Technology, Austria, 2018).
- [32] W. Kohn and L. J. Sham, *Phys. Rev.* **140**, A1133 (1965).
- [33] D. J. Singh and L. Nordström, *Planewaves, Pseudopotentials and the LAPW Method*, 2nd. ed. (Berlin, Germany, 2005).
- [34] A. J. Cohen, P. Mori-Sánchez, and W. Yang, *Chem. Rev.* **112**, 289 (2012).
- [35] K. Burke, *J. Chem. Phys.* **136**, 150901 (2012).
- [36] J. P. Perdew and Y. Wang, *Phys. Rev. B* **45**, 13244 (1992).
- [37] J. P. Perdew, K. Burke, and M. Ernzerhof, *Phys. Rev. Lett.* **77**, 3865 (1996).
- [38] J. P. Perdew, A. Ruzsinszky, G. I. Csonka, O. A. Vydrov, G. E. Scuseria, L. A. Constantin, X. Zhou, and K. Burke, *Phys. Rev. Lett.* **100**, 136406 (2008).
- [39] Z. Wu and R. E. Cohen, *Phys. Rev. B* **73**, 235116 (2006).
- [40] F. Tran, R. Laskowski, P. Blaha, and K. Schwarz, *Phys. Rev. B* **75**, 115131 (2007).
- [41] F. Tran, J. Stelzl, and P. Blaha, *J. Chem. Phys.* **144**, 204120 (2016).
- [42] F. Tran and P. Blaha, *Phys. Rev. Lett.* **102**, 226401 (2009).
- [43] D. J. Singh, *Phys. Rev. B* **82**, 205102 (2010).
- [44] F. Tran and P. Blaha, *J. Phys. Chem. A* **121**, 3318 (2017).
- [45] F. Tran, S. Ehsan, and P. Blaha, *Phys. Rev. Materials* **2**, 023802 (2018).
- [46] A. Belsky, P. Chevallier, E. Mel'chakov, C. Pédrini, P. Rodnyi, and A. Vasil'ev, *Chem. Phys. Lett.* **278**, 369 (1997).
- [47] F. D. Murnaghan, *Proc. Natl. Acad. Sci. USA* **30**, 244 (1944).
- [48] T. Charpin, A package for calculating elastic tensors of cubic phase using WIEN (2006).
- [49] F. Mouhat and F. X. Coudert, *Phys. Rev. B* **90**, 224104 (2014).
- [50] R. Golezorkhtabar, P. Pavone, J. Spitaler, P. Puschnig, and C. Draxl, *Comput. Phys. Commun.* **184**, 1861 (2013).
- [51] A. Togo and I. Tanaka, *Scr. Mater.* **108**, 1 (2015).
- [52] M. Rousseau, P. Daniel, J. Toulouse, and B. Hennion, *Physica B* **234**, 139 (1997).
- [53] M. Born and K. Huang, *Dynamical Theory of Crystal Lattices* (Oxford University Press, Oxford, 1954).
- [54] P. Ghosez, J.-P. Michenaud, and X. Gonze, *Phys. Rev. B* **58**, 6224 (1998).
- [55] S. Ahmed, J. Kivinen, B. Zaporzan, L. Curiel, S. Pichardo, and O. Rubel, *Comput. Phys. Commun.* **184**, 647 (2013).
- [56] W. Zhong, R. D. King-Smith, and D. Vanderbilt, *Phys. Rev. Lett.* **72**, 3618 (1994).
- [57] C.-Z. Wang, R. Yu, and H. Krakauer, *Phys. Rev. B* **54**, 11161 (1996).
- [58] A. C. Garcia-Castro, N. A. Spaldin, A. H. Romero, and E. Bousquet, *Phys. Rev. B* **89**, 104107 (2014).
- [59] R. Wahl, D. Vogtenhuber, and G. Kresse, *Phys. Rev. B* **78**, 104116 (2008).
- [60] J. Tolédano and P. Tolédano, *The Landau Theory of Phase Transitions* (World Scientific, Singapore, 1987).
- [61] E. Salje, *Phase Transitions in Ferroelastic and Coelastic Crystals* (Cambridge University Press, Cambridge, 1990).
- [62] W. Schranz, P. Sondergeld, A. V. Kityk, and E. K. H. Salje, *Phys. Rev. B* **80**, 094110 (2009).
- [63] M. Guennou, P. Bouvier, J. Kreisel, and D. Machon, *Phys. Rev. B* **81**, 054115 (2010).
- [64] M. Guennou, P. Bouvier, G. Garbarino, J. Kreisel, and E. Salje, *J. Phys. Condens. Matter* **23**, 485901 (2011).
- [65] R. A. Cowley, *Phil. Trans. R. Soc. A* **354**, 2799 (1996).
- [66] F. J. Romero, M. C. Gallardo, S. A. Hayward, J. Jiménez, J. del Cerro, and E. K. H. Salje, *J. Phys.: Condens. Matter* **16**, 2879 (2004).

- [67] A. Tröster, W. Schranz, and R. Miletich, *Phys. Rev. Lett.* **88**, 055503 (2002).
- [68] J. Koppensteiner, A. Tröster, and W. Schranz, *Phys. Rev. B* **74**, 014111 (2006).
- [69] A. Tröster and W. Schranz, *Ferroelectrics* **354**, 208 (2007).
- [70] W. Schranz, A. Tröster, J. Koppensteiner, and R. Miletich, *J. Phys. Condens. Matter* **19**, 275202 (2007).
- [71] R. A. Cowley and A. D. Bruce, *J. Phys. C* **6**, L191 (1973).
- [72] B. I. Halperin and P. C. Hohenberg, *Phys. Rev.* **177**, 952 (1969).
- [73] A. D. Bruce, *Adv. Phys.* **29**, 111 (1980).
- [74] M. Campostrini, M. Hasenbusch, A. Pelissetto, P. Rossi, and E. Vicari, *Phys. Rev. B* **65**, 144520 (2002).
- [75] D. J. Bergman and B. I. Halperin, *Phys. Rev. B* **13**, 2145 (1976).
- [76] A. Tröster, *Phys. Rev. Lett.* **100**, 140602 (2008).